[20]A. Onton and R. C. Taylor, Phys. Rev. B **1**, 2587 (1970).

[21]*In detail*: A least-squares linear fit of the Te_0 exciton energy in $In_{1-x}Ga_xP$ to alloy composition gives

$$E_{Te_0}^{2\,°K}(x) = 2.264 + 0.039x \text{ eV}.$$

This extrapolates to 2.303 eV at GaP. If we assume the difference between the indirect band gap and the "extrapolated value" of the exciton energy is similar in InP and GaP, this implies that the indirect Γ_{8v}-X_{1c} gap in InP at $2\,°K$ is 2.299 eV (± 0.030 eV). The error estimate is based on worst-case deviations of experimental data from the least-squares fit. This value lies within experimental error of the value 2.32 ± 0.02 eV determined by Dumke *et al.* (Ref. 14). Because of the large extrapolation involved in the former value, the latter value has been used in Eq. (2). The possibility of a smaller nonlinear deviation of the indirect gap from Eq. (2) is discussed in Sec. IV B.

[22]D. D. Manchon, Jr., and P. J. Dean, in Ref. 10, p. 760.

[23]M. G. Craford, G. E. Stillman, J. A. Rossi, and

N. Holonyak, Jr., Phys. Rev. **168**, 867 (1968).

[24]R. A. Logan, P. J. Dean, H. G. White, and W. Wiegmann, J. Appl. Phys. **42**, 2328 (1971). The authors are grateful to Dr. Logan for sending them a preprint.

[25]A. Onton and T. N. Morgan, Phys. Rev. B **1**, 2592 (1970).

[26]J. Chevallier and H. Rodot report that the N-exciton binding energy extrapolated to GaP from $In_{1-x}Ga_xP$ is lower than that observed in GaP. There is some confusion in their paper about the exciton energy in the $0.9 < x < 1.0$ region of alloy composition. We have observed the same spectrum and find the principal exciton recombination spectral peak at 2.3125 eV for $x = 0.990$, and $(dE/dx) = 0.48$ (eV/unit mole fraction) for $0.990 \geq x \geq 0.980$ [A. Onton, T. N. Morgan, and T. S. Plaskett (private communication)]. These results are consistent with those of Logan *et al.* (Ref. 24). However, the value of dE/dx we find is considerably larger. The conclusion Chevallier and Rodot reach on the location of the conduction-band crossover, based on the spectrum attributed to a sample with composition $x = 0.64$, is entirely inconsistent with the results we report in this paper.

Heliconlike Wave Propagation in Powdered Semiconductors at Microwave Frequencies*

Frank L. Galeener[†] and Jacek K. Furdyna

Department of Physics, Purdue University, Lafayette, Indiana 47907

(Received 8 March 1971)

Experiments on the propagation of 35-GHz microwaves in magnetically biased powdered narrow-gap semiconductors are described and their major features explained by a simple single-scattering theory derived in the paper. Attention is restricted to grains much smaller than the wavelength of the incident waves. The grains are idealized to spheres which are gyroelectric because of the applied dc magnetic field. The scattering and absorption properties of an isolated gyroelectric sphere are analyzed using an *ad hoc* assumption that, under a given normal-mode excitation, a gyroelectric sphere can be represented by an *isotropic* sphere described by the bulk permittivity associated with that excitation. This approach explains the main features of the data in terms of particle-size-dependent resonances and high-field size-independent absorption. Variations of resonance position and strength with powder grain size, size distribution, temperature, and carrier concentration are easily understood using the single-particle expressions. Low-temperature microwave transmission in InSb and InAs powders shows well-resolved Shubnikov–de Haas oscillations at field values in remarkably good agreement with theory.

I. INTRODUCTION

We have investigated experimentally and theoretically the problem of electromagnetic wave propagation in powdered narrow-gap semiconductors in the presence of an externally applied magnetic field.[1-3] We report experiments carried out in the microwave region (35 GHz) on granulated high-mobility materials which exhibit a strong and striking dependence of wave-propagation properties on the applied dc magnetic field. A complete quantitative description of the data demands a rather sophisticated analysis, entailing particle-particle interactions and the effect of irregular particle shape, beyond the scope of the present work. Nevertheless

it will be shown that all observed qualitative features of the transmissivity can be explained on the basis of a simple single-scattering theory whose essentials are presented.

It is clear that the study of electromagnetic behavior of powders provides an opportunity to investigate transport properties of materials available in granular form, as well as the effect of small size on these properties. In addition, it poses a series of problems in electrodynamics and scattering theory. Understanding of this rather complex problem is therefore highly worthwhile in general. In our discussion we shall emphasize the aspects of interest to the solid-state physicist and shall endeavor, whenever possible, to emphasize the relationship
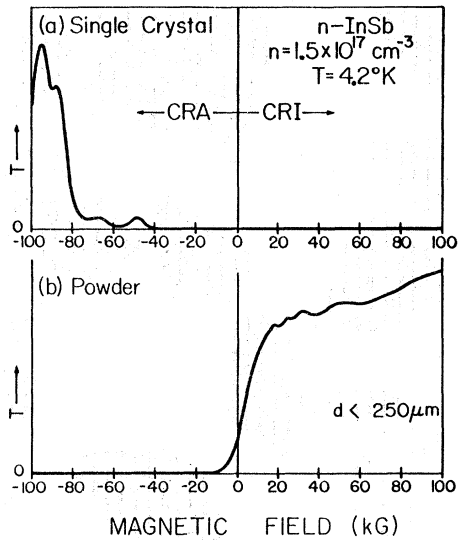
FIG. 1. Transmitted power of circularly polarized microwaves through n-type InSb as a function of longitudinal dc magnetic field. Curve (a) is for a single-crystal slab 1 mm thick, and curve (b) is for an unsieved powder of the same material, 8 mm thick. Note the pronounced reversal of "handedness." Peak transmissivity is comparable in both cases, approximately 0.1%.

of the effects observed in powders to dc transport parameters, surface impedance, and helicon waves.

Wave propagation in powders reveals some rather unexpected effects, as is illustrated in Fig. 1, which compares the transmission of circularly polarized microwaves in Faraday configuration through (a) a single-crystal slab of n-type InSb and (b) a slab-shaped region of the same material in powdered form. The positive and negative field values correspond to opposite senses of electron cyclotron orbits relative to the sense of circular polarization of the incident waves. When the orbital motion is in the same sense as the polarization of the wave, we refer to the wave as cyclotron resonance active (CRA), corresponding to negative fields in the figure; when the cyclotron motion is opposite to the circular polarization, the wave is referred to as cyclotron resonance inactive (CRI). The upper curve is well understood in terms of helicon wave propagation in semiconductor slabs.[4] The lower curve was not understood until the dimensional resonance mechanism, to be elucidated in this paper, was conceived. The mystery was the apparent "reversal of handedness" of the medium after it is powdered; as the figure shows, the powder transmits waves of the circular polarization rejected by the solid sample, and is opaque to waves of the circular polarization that the solid sample transmits.

II. EXPERIMENTAL DETAILS

All of the experimental results reported in this paper involve microwave transmission through powders in the Faraday configuration, where the propagation direction $\vec{k}$ of the incident circularly polarized waves is parallel to the applied dc magnetic field $\vec{B}$, and the electric vector of the wave is perpendicular to $\vec{B}$.

The basic experimental arrangement is shown in Fig. 2. For measurements of transmitted signal strength, the bridge arm is effectively removed by large values of attenuation in the attenuator A. The 35-GHz microwaves propagate in a rectangular waveguide to a circular polarizer above the Dewar, and the circularly polarized waves travel in the TE_{11} mode along a cylindrical guide to the powder sample located at the center of a Bitter solenoid, as shown. The powder sample is loosely packed in a short section of circular guide, typically less than 1 cm long, and forms a slab-shaped region contained by two Teflon or Mylar disks. Energy transmitted through the powder traverses a circular-to-rectangular waveguide transition and proceeds through the rectangular waveguide turn-around T to the detector D. Reflection (at the transition) of transmitted energy having the polarization not admitted by the rectangular guide is minimized by an absorbing vane.

Measurements were performed on powders of n-type InSb, InAs, HgTe, and HgSe of various carrier concentrations, as well as on intrinsic InSb and HgTe, in the temperature range from 4.2 to 380 °K and in fields up to 150 kG. These materials are characterized by high electron mobilities and spherical or nearly spherical conduction bands.

All of the powders were formed by crushing previously characterized single-crystal material in a mortar and pestle. Most of the powder samples were size-fractioned by passing between two precision sieves, and the resultant range of particle sizes is specified as $d_{min} < d < d_{max}$, where d_{min} and d_{max} are the nominal aperture dimensions of the smaller and larger mesh sieves, respectively. Figure 3 illustrates very well the typical shape of the particles, in this case an InAs powder whose size limits are $177 < d < 250$ μm. Notice that the crushing and sifting process results in fairly compact particles; very few have the relative dimensions of disks or needles. This, along with the randomness inherent in a powder, provides some preliminary justification for our later idealization of the particles to spheres, even though the grains are highly angular and rarely have smoothly curved surfaces.

III. THEORETICAL CONSIDERATIONS

The major features of our results can be understood in terms of a size-dependent resonant inter-
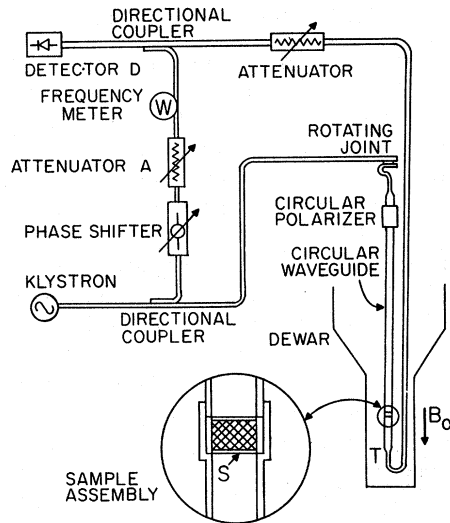
FIG. 2. Apparatus used for measuring 35-GHz micro-wave transmission through single crystal and powdered semiconductors.

FIG. 3. Typical shape of the particles in an InAs powder with nominal size range $177 < d < 250\,\mu m$. Note the absence of noncompact shapes such as disks or needles.

action of heliconlike waves with the individual particles. We imagine each grain to be replaced by a spherical particle of the material from which the powder was made, having volume approximately equal to that of the grain. As an approximation to the experimental arrangement, we consider a slab-shaped array of these spherical scatterers, illuminated by a circularly polarized *plane* wave normally incident on the slab and propagating parallel to the applied magnetic field $\vec{B}$, also normal to the slab. This configuration, often referred to as the Faraday geometry, is depicted in Fig. 4.

It is clear that even with spherical particles and plane-wave excitation the microwave electric field acting on each particle in the random array is not perfectly transverse to $\vec{B}$ nor is it perfectly circularly polarized. This is, in part, another way of saying that the particles interact, the response of a given particle depending on the response of the others. Nevertheless, we wish to limit our attention to the simplest possible model for the observed phenomena and so we treat the assembly as a group of *noninteracting* scatterers, each of which extracts an amount of energy from the wave proportional to its electromagnetic cross section. Under these assumptions, the task which remains is to consider the scattering of electromagnetic waves by an isolated spherical particle of arbitrary size, consisting of gyroelectric material described in the bulk by a tensor permittivity of the form

$$\overleftrightarrow{\epsilon} = \begin{pmatrix} \epsilon_{xx} & \epsilon_{xy} & 0 \\ -\epsilon_{xy} & \epsilon_{xx} & 0 \\ 0 & 0 & \epsilon_{zz} \end{pmatrix} . \qquad (1)$$
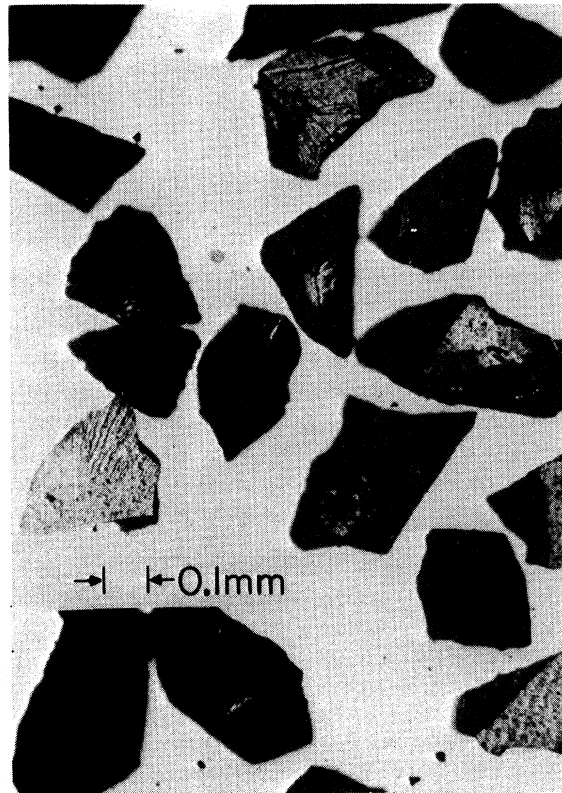
An exact solution of the scattering of a plane wave by a gyroelectric (or gyromagnetic) sphere of arbitrary size is unavailable and appears to be quite difficult. The theoretical problem has been discussed by Epstein,[5] Nagelberg,[6] and others.[7] We have devised an *ad hoc* approximate solution which is successful in explaining most features of the experiments reported on single spheres by Cardona and
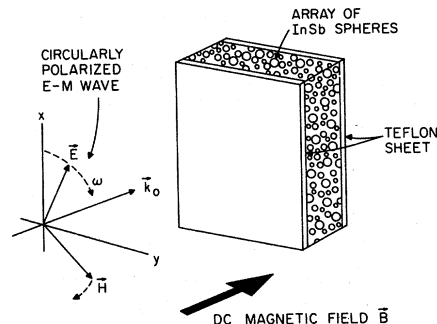

FIG. 4. Idealized picture of the experiments, depicting transmission of circularly polarized plane waves through a slab-shaped region of spherical particles in Faraday geometry.

Rosenblum,[8] and allows a simple quantitative interpretation of our powder results.

It is well known that the gyroelectric tensor (1) can be diagonalized in the coordinate system

$$2^{-1/2}(\hat{x}+i\hat{y}) , \quad 2^{-1/2}(\hat{x}-i\hat{y}) , \quad \hat{z} ,$$

resulting in the respective diagonal components

$$\epsilon_{+} \equiv \epsilon_{xx}+i\epsilon_{xy} , \quad \epsilon_{-} \equiv \epsilon_{xx}-i\epsilon_{xy} , \quad \epsilon_{z}=\epsilon_{zz} . \tag{2}$$

Each of these principal values describes in effect the response of the bulk medium to the separate excitation by one of the three normal modes: the two circularly polarized fields E_{+} and E_{-}, transverse to $\vec{B}$, and the linear polarization E_{z} parallel to the dc magnetic field. Our approximation is, briefly, as follows: In the presence of a given circularly polarized excitation transverse to $\vec{B}$ (say E_{+}), we calculate the scattering by an anisotropic (gyroelectric) particle as if it were an isotropic sphere described by one of the principal values of Eq. (2) (say ϵ_{+}, corresponding to the E_{+} excitation). This enables us to apply the powerful Mie-Debye theory of electromagnetic scattering by a homogeneous isotropic sphere.[9-11] In this simplest approach to our powder data, we attempt to calculate only the strength of the transmitted wave, and accordingly consider only the absorption cross section of the Mie theory in a quantitative manner.

A. Scattering by an Isotropic Sphere

The Mie theory involves expansion of the interior and scattered waves into multipole components of two kinds: electric waves and magnetic waves. This nomenclature is convenient because the near fields of each type of wave correspond to the familiar static field configurations having the same name; for example, the lowest magnetic multipole wave has near fields resembling a *static* magnetic dipole field configuration. The strengths of the scattered multipole waves are given by the following coefficients:

$$^{m}S_{n} = \frac{j_{n}(Z)[Z_{0}j_{n}(Z_{0})]' - j_{n}(Z_{0})[Zj_{n}(Z)]'}{j_{n}(Z)[Z_{0}h_{n}^{1}(Z_{0})]' - h_{n}^{1}(Z_{0})[Zj_{n}(Z)]'} , \tag{3}$$

$$^{e}S_{n} = \frac{\kappa j_{n}(Z)[Z_{0}j_{n}(Z_{0})]' - j_{n}(Z_{0})[Zj_{n}(Z)]'}{\kappa j_{n}(Z)[Z_{0}h_{n}^{1}(Z_{0})]' - h_{n}^{1}(Z_{0})[Zj_{n}(Z)]'} , \tag{4}$$

where

$$Z \equiv ka = X+iY , \quad k^{2} \equiv (\alpha+i\beta)^{2}=k_{0}^{2}\kappa , \quad \text{and } Z_{0}=k_{0}a .$$

In these expressions, $\kappa \equiv \kappa'+i\kappa''$ is the complex dielectric constant of the sphere, a is the radius of the sphere, $k_{0} \equiv \omega/c$ is the free-space propagation constant of the incident wave, and k is the interior complex wave propagation constant, the same as for plane waves in an infinite sample of the material from which the sphere is made. The functions $h_{n}^{1}(\zeta)$ and $j_{n}(\zeta)$ are the spherical Hankel functions

of the first kind and the spherical Bessel functions, respectively, both of order n.[12] The subscript n indicates the multipole order by means of the usual 2^{n}-pole nomenclature. The presuperscripts m and e denote magnetic and electric waves, respectively.

Three kinds of cross sections are encountered in the scattering analysis: the absorption cross section Σ_{abs}, the scattering cross section Σ_{sca}, and the extinction cross section Σ_{ext}. As outlined in Stratton,[9] one finds that the cross sections can be evaluated in terms of the scattered wave coefficients alone:

$$\Sigma_{sca} = \frac{2\pi}{k_{0}^{2}} \sum_{n=1}^{\infty} (2n+1)(|{}^{e}S_{n}|^{2}+|{}^{m}S_{n}|^{2}) , \tag{5}$$

$$\Sigma_{ext} = \frac{2\pi}{k_{0}^{2}} \sum_{n=1}^{\infty} (2n+1)[\mathrm{Re}({}^{e}S_{n})+\mathrm{Re}({}^{m}S_{n})] , \tag{6}$$

$$\Sigma_{abs} = \Sigma_{ext} - \Sigma_{sca} . \tag{7}$$

In practice, it is easiest to evaluate the extinction cross section, according to Eq. (6), which measures the total power extracted from the incident wave through absorption and scattering by the particle. Calculations using parameters corresponding to the experiments analyzed in this paper show that much more energy is absorbed than scattered, and we can essentially equate Σ_{abs} to Σ_{ext}.

1. Dominance of Dipole Terms

In all the experiments, the powder particles are much smaller than the wavelength of the incident microwaves. Thus, we can evaluate the scattered wave coefficients, Eqs. (3) and (4), in the limit $Z_{0} \equiv k_{0}a \ll 1$. Series expansion of $j_{n}(Z_{0})$ and $h_{n}^{(1)}(Z_{0})$ appropriate for small Z_{0} simplifies the scattered wave coefficients to[12]

$$^{m}S_{n} \approx \frac{(2n+1)j_{n}(Z)-Zj_{n-1}(Z)}{Zj_{n-1}(Z)} F_{n}(Z_{0}) , \tag{8}$$

$$^{e}S_{n} \approx \frac{[(n+1)\kappa+n]j_{n}(Z)-Zj_{n-1}(Z)}{n(\kappa-1)j_{n}(Z)+Zj_{n-1}(Z)} F_{n}(Z_{0}) , \tag{9}$$

where

$$F_{n}(Z_{0}) = \frac{-i}{2n+1} \left(\frac{2^{n}n!}{(2n)!} \right)^{2} Z_{0}^{2n+1} .$$

Two important observations are easily made concerning these results. First, the condition $Z_{0} \ll 1$ separates the Z_{0} dependence from the Z dependence of the scattering coefficients. Second, the Z_{0}-dependent functions $F_{n}(Z_{0})$ decreases *very* rapidly with the multipole order n. In particular, the ratio of the second to the first is $\frac{1}{15}(k_{0}a)^{2}$, while the ratio of the third to the first is $\frac{1}{525}(k_{0}a)^{4}$. Thus, one can neglect quadrupole ($n=2$) and higher-order contributions relative to dipole ($n=1$) term. We conclude,

therefore, that dipole scattering dominates the isolated-scatterer model everywhere, and we assume that it also dominates the powder scattering.

The dipole-scattered wave coefficients are immediately found from Eqs. (8) and (9) to be

$$^mS_1 \approx \frac{3j_1(Z) - Zj_0(Z)}{Zj_0(Z)} F_1(Z_0) ,$$ (10)

$$^eS_1 \approx \frac{(2\kappa + 1)j_1(Z) - Zj_0(Z)}{(\kappa - 1)j_1(Z) + Zj_0(Z)} F_1(Z_0) ,$$ (11)

where $F_1(Z_0) = -\frac{1}{3}i (k_0a)^3$, and the range of Z is unlimited.

2. Dimensional Resonance Condition

We are interested in possible resonances of the scattered wave coefficients, hence the cross sections. To estimate the conditions under which resonances occur, we first examine the lossless limit, where κ'', β, and Y vanish, and look for infinites in (10) and (11). Since both numerators are finite for all X, the singularities arise only from zeros of the denominators.

For the magnetic dipole, the condition is simply

$$j_0(X) = 0 .$$ (12)

This has an infinity of solutions,[12] denoted by M_{1m}, which represent the values of X at which *magnetic* dipole dimensional resonances occur. The exact solutions of (12) are $M_{1m} = m\pi$, so that the first few numerical values are

$$M_{11} = 3.14, \quad M_{12} = 6.28, \quad M_{13} = 9.42, \quad \dots .$$

For the electric dipole, the resonance condition [from Eq. (11)] is

$$j_1(X) = -Xj_0(X)/(\kappa' - 1) .$$ (13)

The real part of the dielectric constant appropriate to our systems is quite large when dimensional resonance occurs, $\kappa' \gg 1$. A graphical study of Eq. (13) then reveals that its solutions are very nearly given by the zeros of $j_1(X)$. This function has an infinity of solutions,[12] which we denote by E_{1m}. The first few solutions of $j_1(X) = 0$, corresponding to *electric dipole* resonance and arranged in ascending order, follow:

$$E_{11} = 4.493 , \quad E_{12} = 7.725 , \quad E_{13} = 10.90, \quad \dots .$$

We speak of these resonances as dimensional because they occur at values of α which depend on the sphere dimension a. Roughly, their occurence corresponds to the exact fitting of spherical wave patterns into the interior of the particle. For example, the "lowest" magnetic dimensional resonance occurs when the interior wavelength equals the sphere diameter, since the condition $M_{11} = \pi$ is equivalent to $\lambda = 2a$.

3. Strength of Dimensional Resonance

It is difficult to treat the scattering coefficients when there is appreciable loss, i.e., when $Y \gtrsim X$. However, if we assume Y sufficiently small, we can obtain approximate expressions for the coefficients at resonance:

$$^mS_1 \approx (k_0a)^3/\overline{XY} = 2(k_0a)/\overline{\kappa}'' ,$$ (14)

$$^eS_1 \approx (k_0a)^5/\overline{XY} = 2(k_0a)^3/\overline{\kappa}'' \ll {}^mS_1 .$$ (15)

In these expressions, $\overline{X}$, $\overline{Y}$, and $\overline{\kappa}''$ represent values of X, Y, and κ'' evaluated when dimensional resonance obtains. Expressions (14) and (15) are borne out by computer calculations using the complete coefficients (3) and (4).

4. Strength of Absorption Under Small Skin Depth Conditions

Sharp and strong dimensional resonances occur only when the skin depth of the waves inside the particle is large compared to the particle size, i.e., when $\beta a \ll 1$. We shall also be interested in the response of spherical particles when the skin depth is small compared to particle size, when $\beta a > 1$. In particular, when one treats the region $1 \leq Y \gg X$ (typically associated with the condition $\kappa' < 0$, $|\kappa'| \gg \kappa''$, as will be evident in Sec. III A 1), one finds that the magnetic and electric dipole extinction cross sections are given by

$$^m\Sigma_{ext} \approx \frac{9}{2} (k_0V)\frac{X}{Y^2} \approx 3(\pi a^2)\frac{\kappa''}{|\kappa'|^{3/2}} ,$$ (16)

$$^e\Sigma_{ext} \approx 3(\pi a^2)\frac{\kappa''}{|\kappa'|^{3/2}}(k_0a)^2 \ll {}^m\Sigma_{ext} .$$ (17)

Since $k_0a \ll 1$ in our experiments, absorption under these conditions will also be dominated by the *magnetic dipole* excitation.

We remark parenthetically that the coefficient $\kappa''/|\kappa'|^{3/2}$ also appears in the absorption coefficient A of a plane wave normally incident on a plane infinite half-space, which under similar conditions ($\beta \gg \alpha$, $\beta \gg k_0$) is given by

$$A \cong \frac{4k_0\alpha}{(k_0 + \alpha)^2 + \beta^2} \approx \frac{4k_0\alpha}{\beta^2} \approx \frac{\kappa''}{|\kappa'|^{3/2}} ,$$ (18)

as can be readily verified. Equations (16) and (17) emphasize, therefore, the similarity of powder measurements to surface-impedance experiments, which are used to measure A.

B. Permittivity and Wave Propagation Constants in Bulk

Most of our experimental results can be adequately discussed in terms of the semiclassical Drude model for the bulk dielectric constants of the material from which the powder is formed. The shortcomings of the model, relevant to our range of interest, will be briefly presented later.

According to the Drude model, the principal dielectric constants of a semiconductor consisting of electrons (n) and holes (p) are given by

$$\kappa_\pm \equiv \kappa_l + \frac{i}{\omega\epsilon_0}(\sigma_{xx} \pm i\sigma_{xy})$$

$$= \kappa_l + \frac{i}{\omega\epsilon_0}\left(\frac{ne\mu_n}{1 - i(\omega\tau_n \mp \mu_n B)} + \frac{pe\mu_p}{1 - i(\omega\tau_p \pm \mu_p B)}\right) ,$$

(19)

where κ_l is the lattice dielectric constant, n and p are the electron and hole concentrations, respectively, and μ_n and μ_p, τ_n and τ_p are their mobilities and collision times, respectively. We have also at this point reexpressed the dielectric function in terms of components of the corresponding high-frequency magnetoconductivity tensor $\sigma_{ij}(\omega, B)$. Expressions involving σ_{ij} in Eq. (19) are macroscopic definitions, not subject to semiclassical restrictions, and are presented at this point for future convenience. The cases designated by $(\pm)$ correspond to opposite senses of circular polarization about the direction of the applied magnetic field: The $(+)$ sign refers to the cyclotron-resonance-active (CRA) configuration for electrons, and the $(-)$ sign corresponds to the cyclotron-resonance-inactive (CRI) polarization, as discussed in the Introduction. Clearly, the CRA configuration for electrons is the CRI configuration for holes. However, since most of the phenomena described herein are governed by the electron motion, we have throughout this article designated polarization configurations as CRA and CRI *with respect to the response of electrons only*.

1. Electrons Only: Helicon Limit

Most of the semiconductor materials studied were n type, so that the contributions of holes to Eq. (19) can be neglected $(p\mu_p \ll n\mu_n)$. Furthermore, except at very low magnetic fields, electron mobilities were high enough to satisfy the condition

$$\mu B \gg \omega\tau \text{ and } 1,$$

(20)

which means that the fields of interest were well removed from the cyclotron resonance field. Under these conditions, it can be shown that

$$|\sigma'_{xy}(\omega, B)| \approx |\sigma_{xy}(0, B)| \gg |\sigma''_{xx}(\omega, B)| ,$$

$$|\sigma'_{xx}(\omega, B)| \approx |\sigma_{xx}(0, B)| \gg |\sigma''_{xy}(\omega, B)| ,$$

(21)

$$|\sigma'_{xy}| \gg |\sigma'_{xx}| ,$$

where single and double primes denote real and imaginary parts of $\sigma_{ij}(\omega, B)$, and $\sigma_{ij}(0, B)$ represent components of the corresponding dc magnetoconductivity tensor. These relations follow immediately from the Drude model, but are actually much more general,[13] and will prove convenient for discussion

of measurements under conditions where the semiclassical form is inadequate. Under conditions (20), real and imaginary parts of Eq. (19) (designated $\kappa'_\pm$ and $\kappa''_\pm$, respectively) assume the simple forms

$$\kappa'_\pm \approx \kappa_l \mp \frac{\sigma_{xy}(0, B)}{\omega\epsilon_0} \approx \kappa_l \pm \frac{ne}{\omega\epsilon_0 B} \approx \pm \frac{ne}{\omega\epsilon_0 B} ,$$

(22)

$$\kappa''_\pm \approx \frac{\sigma_{xx}(0, B)}{\omega\epsilon_0} \approx \frac{ne}{\omega\epsilon_0\mu_n B^2} = \frac{|\kappa'_\pm|}{\mu_n B} ,$$

(23)

where the last form of Eq. (22) is subject to the additional condition $ne/(\omega\epsilon_0 B) \gg \kappa_l$, referred to as the "helicon limit," which is satisfied by the parameters involved in the present experiments. In this parameter range the wavelength of the CRA waves, described by κ_+, will be much shorter than their free-space wavelength, by as much as a factor $\sqrt{\kappa'} \approx 10^2$. In this way, 8-mm microwaves may be reduced to 80-μm waves inside the powder grains (which is the order of the grain diameter).

It is readily seen that for the CRA polarization, where $\kappa' \gg \kappa'' > 0$, the propagation and attenuation coefficients become

$$\alpha \equiv k_0\left(\frac{|\kappa| + \kappa'}{2}\right)^{1/2} \approx k_0\left(\frac{|\sigma'_{xy}|}{\omega\epsilon_0}\right)^{1/2} \approx k_0\left(\frac{ne}{\epsilon_0\omega B}\right)^{1/2} ,$$

(24)

$$\beta \equiv k_0\left(\frac{|\kappa| - \kappa'}{2}\right)^{1/2} \approx \frac{k_0}{2}\frac{\sigma'_{xx}}{(\omega\epsilon_0|\sigma'_{xy}|)^{1/2}} \approx \frac{1}{2}\frac{\alpha}{\mu B} ,$$

(25)

in the helicon range. The final form on the right-hand side corresponds to the Drude model.

In the CRI case, the analytic expressions for α and β in terms of transport parameters are interchanged. It is clear that, in the helicon limit, CRI fields correspond to large wavelengths and small skin depths, while CRA fields correspond to wavelengths of the order of particle dimensions and skin depths larger than the particle size.

2. Limitations of Drude Model in Helicon Approximation

Although the dominant features of our observations can be satisfactorily described in terms of the Drude model, it must be pointed out that the semiclassical treatment can be quite inadequate in the helicon limit. Arguing empirically, we recall that the semiclassical model predicts saturation in the closely related problem of transverse dc magnetoresistance,

$$\rho_\perp \equiv \frac{\sigma_{xx}(0, B)}{\sigma^2_{xx}(0, B) + \sigma^2_{xy}(0, B)}$$

(26)

under condition (20) in extrinsic materials; such saturation is not observed experimentally in the narrow-gap semiconductors of interest here.[14,15] Theoretically, the classical model is expected to

fail at very high magnetic fields where only a few low quantum numbers are involved, i.e., when the electron energy does not greatly exceed $\hbar\omega_c$.[16] Because of the small effective masses characteristic of narrow-gap materials, the latter condition applies to our experiments even at room temperature, at least in the high-field region.

It is instructive to examine the effects of orbital quantization on the individual components of the magnetoconductivity tensor, in terms of which κ_+ is expressed in Eq. (19). We assert that, under condition (20), the set of inequalities (21) is still expected to hold even in the presence of strong orbital quantization.[13,17] It is thus only necessary to examine quantum effects in the dc behavior of $\sigma_{xy}(0, B)$ and $\sigma_{xx}(0, B)$, which, respectively, determine $\kappa'_\pm$ and $\kappa''_\pm$ in the helicon limit, as given in Eqs. (22) and (23).

The effect of orbital quantization on $\sigma_{xy}(0, B)$ (and thus $\kappa'_\pm$) is very weak, and rigorous quantum mechanical treatment of the high-field region yields[16,18]

$$\sigma_{xy}(0, B) = ne/B , \qquad (27)$$

which is identical to the semiclassical result. The semiclassical form of all dispersive features, including α for the CRA mode developed in Sec. III B 1, is therefore expected to remain valid.

The behavior of $\sigma_{xx}(0, B)$ under quantum conditions on the other hand, differs markedly from the form derived via the Drude model. The Shubnikov–de Haas effect in degenerate media, observed in the "oscillatory regime"[16,18] ($\zeta_F > \hbar\omega_c \gg k_B T$, where $k_B T$ is the thermal energy and ζ_F is the Fermi energy at $B = 0$) is well known and will be dealt with in greater detail in Sec. IV C 3. Similarly in the "quantum limit"[16,18] ($\hbar\omega_c > k_B T$ for nondegenerate systems and $\hbar\omega_c > \zeta_F$ for degenerate statistics), which is satisfied or nearly satisfied in the upper-field range of our measurements, the magnetic field and temperature dependence of $\sigma_{xx}(0, B)$ (and thus $\kappa''_\pm$) becomes a strong function of the scattering mechanism and carrier statistics involved. This dependence has been studied theoretically in the extreme quantum limit ($\hbar\omega_c \gg \zeta_F$ or $k_B T$) and tabulated for various scattering mechanisms.[16,18] It is noted that, with the exception of ionized impurity scattering in nondegenerate systems, $\sigma_{xx}(0, B)$ always drops off less rapidly than B^{-2} with increasing field, and in many instances actually *increases* with B, in sharp contrast with the semiclassical result. Thus no saturation of transverse magnetoresistance is expected when orbital quantization is effective and, for our purposes, the Drude expression for $\kappa''_\pm$ is much too small in the high-field region.

We finally remark that other mechanisms can also be responsible for the absence of saturation of $\rho_\perp(0, B)$, even though $\sigma_{xy}(0, B)$ behaves "classically" in the high-field domain. Microscopic inhomogeneities and the presence of comparatively heavy minority carriers have frequently been invoked as alternative explanations,[15] and it is actually not always clear which of the mechanisms is dominant. We note, however, that under conditions (21) and with the classical behavior of $\sigma_{xy}(0, B)$ empirically established, we can write

$$\sigma_{xx}(0, B) \approx \rho_\perp \sigma_{xy}{}^2(0, B) \approx \rho_\perp(ne/B)^2 . \qquad (28)$$

We then immediately conclude that in materials in which $\rho_\perp$ does not saturate, for whatever reasons, $\sigma_{xx}(0, B)$ (and therefore $\kappa''_\pm$) falls off at a slower rate than predicted semiclassically, although the Drude calculation of $\kappa'_\pm$ remains valid. These remarks will be essential for discussing the line shape of powder transmission data presented in subsequent sections.

C. Scattering by Magnetoplasma Sphere

1. *Dimensional Resonance*

As discussed earlier, we approximate the anisotropic sphere scattering by the isotropic scattering solution, using the principal value of the dielectric constant appropriate for the incident polarization. Thus for circularly polarized excitation of a magnetoplasma sphere by a wave propagating along the applied field $\vec{B}$, we evaluate the Mie coefficients (3) and (4) using propagation constants k_+ or k_- obtained from the principal dielectric constant (19). Figure 5 illustrates the result of an exact (computer) calculation[19,20] using parameters typical of one of our n-type InAs samples. There are *two* curves plotted versus applied magnetic field: The upper curve is a specific extinction cross section, while the lower curve is the specific scattering cross section. The weakness of the peak in the lower curve, seen at -55 kG, indicates (as mentioned before) that during dimensional resonance in these systems absorption dominates scattering. Both curves are the *sum* of electric *and* magnetic dipole contributions and are termed specific because the electromagnetic cross sections are divided by the geometric cross section πa^2. The two prominent lines correspond to magnetic dipole dimensional resonances. The electric dipole resonances are too weak to be seen in comparison with the magnetic ones, as was indicated earlier. Quadrupole contributions were also calculated and are much too small to be seen on the scale of Fig. 5.

Thus, in the region where dimensional resonance can occur, we need evaluate only the magnetic dipole extinction cross section in the CRA helicon limit. The resonance condition is $\alpha a = M_{1m}$. In the helicon limit, using Eq. (24), this can be solved for the resonant fields

$$B_r = -\mu_0 en\omega(a/m\pi)^2 , \qquad (29)$$

where $m = 1$ corresponds to a one-wavelength (fundamental) dimensional resonance, $m = 2$, a two-wavelength dimensional resonance, and so on. The strength of these resonances is measured by the extinction cross section calculated using Eqs. (6), (14), and (23) with the result that

$$\overline{\Sigma}_{ext} = \frac{12\pi k_0 a}{k_0^2 \overline{\kappa}_{CRA}^{\prime\prime}} = \frac{12\pi(k_0 a)}{\mu_0 e n \omega} \; \mu B_r^2$$

$$= 12\pi\mu_0\omega(k_0 a)\left(\frac{a}{m\pi}\right)^4 ne\mu \; , \qquad (30)$$

where the bar over a quantity denotes that the quantity is evaluated at resonance. The final form is obtained from the Drude expression for κ'', via Eq. (29). We see therefore that, according to the Drude model, the strength of dimensional resonance increases as the fifth power of the particle size, and decreases as the inverse fourth power of the order of the resonance. In view of this latter fact, the one-wavelength dimensional resonance cross section dominates two-wave dimensional resonance by a factor of 16 (see Fig. 5). Under conditions where the semiclassical model is not expected to be valid, the strength of the resonance will be given by the appropriate form of $\overline{\sigma}'_{xx} \equiv \sigma_{xx}(0, B_r)$, which can be taken directly from dc transport theory, as discussed in Sec. III B 2.

2. Magnetoplasma Resonance

As we have shown, dimensional resonance takes place when the bulk dielectric constant is large and mostly real and positive. Another resonance in the scattering coefficients occurs when the bulk dielectric constant is small and negative.[21] From a scattering theory point of view, this resonance is seen

in simplest form for particles satisfying the Rayleigh limit[22] $k_0 a \ll 1$, $|ka| \ll 1$, which means that the external and internal fields are essentially uniform over the particle dimensions. Using these conditions in Eqs. (3) and (4), one finds that the electric dipole extinction cross section is given by

$$\Sigma_{ext} \approx 12\pi(k_0 a)a^2 \frac{\kappa''}{(\kappa' + 2)^2 + (\kappa'')^2} \; , \qquad (31)$$

while the magnetic dipole extinction cross section is much smaller, approximately by a factor $(k_0 a)^2$.

Equation (31) has been discussed in Ref. 21, where it is pointed out that the resonance which occurs when $\kappa' = -2$ is identical with the magnetoplasma resonance first discussed in depolarization language by Dresselhaus, Kip, and Kittel.[23] In the high-field limit for a system of electrons only, the magnetoplasma resonance condition $\kappa' = -2$ yields resonance at the CRI field

$$B_r = ne/\omega\epsilon_0(\kappa_l + 2) \; , \qquad (32)$$

which is independent of particle size.

Magnetoplasma resonance in a multicarrier system can differ significantly from the behavior expected in materials involving one-band conduction. Approximate expressions taking into account the effect of an equal number of electrons and low-mobility holes have been presented elsewhere,[3] with emphasis on the broadening effects (dominant damping) due to the heavy holes, which determine κ'' at high fields.[24]

Returning to the system of electrons only, we finally remark that, while the expression for κ' calculated semiclassically remains valid under quantum conditions discussed in Sec. III B 2, κ'' is in general expected to be significantly larger at high

$$n = 2.7 \times 10^{16} \, cm^{-3}$$
$$K_L = 14.5$$
$$m^* = 0.026 \, m_0$$
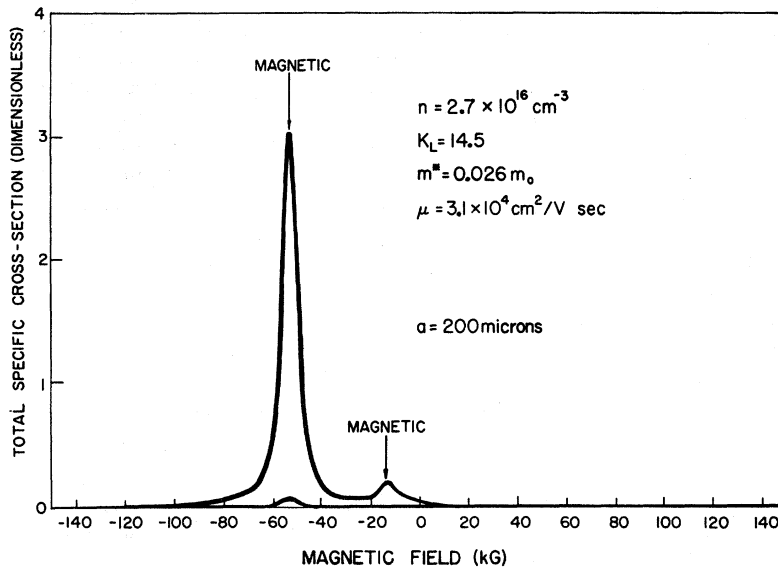$$\mu = 3.1 \times 10^4 cm^2/V \; sec$$

$$a = 200 \, microns$$

FIG. 5. Theoretical specific dipole cross-section spectra for a single sphere of n-type InAs. The lower curve is scattering while the upper is scattering plus absorption. In this case, electric dipole contributions are too weak to give observable structure. The peaks represent one-wavelength (-55 kG) and two-wavelength (-15 kG) dimensional resonances in the magnetic dipole cross sections.
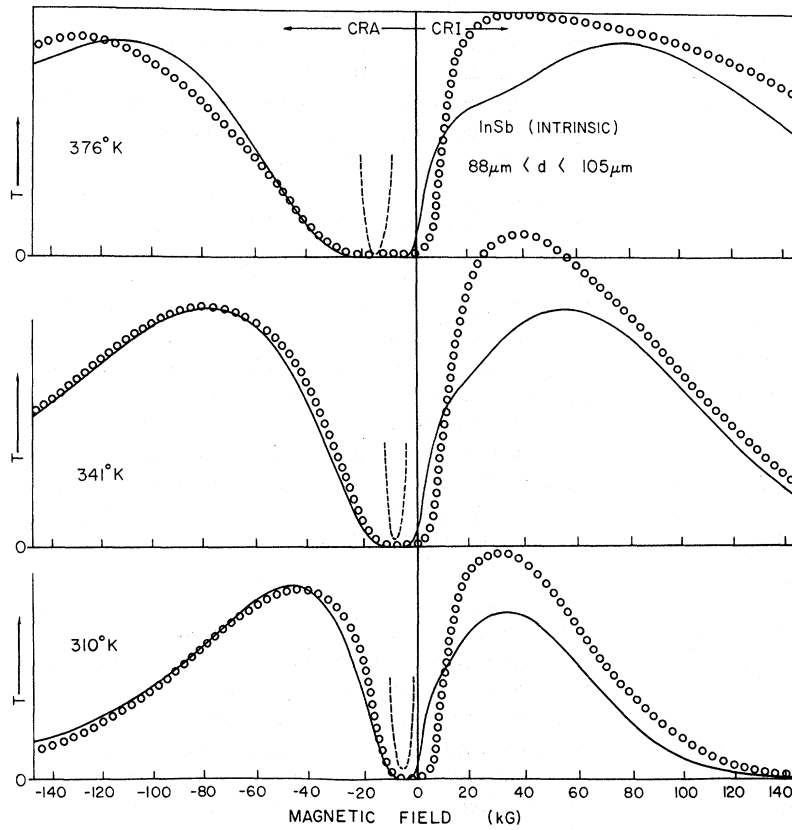
FIG. 6. Temperature dependence of the transmitted microwave power T (relative scale) through an intrinsic InSb powder. The central absorption line, shown at increased gain by the dashed curves, is known to be size dependent. The circles represent theoretical transmissivities, computed for a semiclassical electron-hole plasma, as discussed in Sec. IV B 1.

fields than the corresponding semiclassical value. Thus in an extrinsic material we do not expect a shift in the resonant field, defined by Eq. (32), but [as is readily seen from Eq. (31)] we can expect an enormous broadening of the resonance due to the behavior of κ'' in the quantum limit. Such broadening is empirically similar to the effect of the heavy holes just mentioned, but arises in this case from the mechanism of orbital quantization.

IV. EXPERIMENTAL RESULTS AND INTERPRETATION

In this section we report the experimental results obtained on powders and interpret the main features in terms of the single-particle scattering theory just presented. Quantitative emphasis is on the dimensional resonance effects which are expected in the CRA configuration (for electrons), since only for that field orientation is the internal wavelength small enough to fit inside a powder grain while the internal skin depth is large enough to allow the interior waves to traverse the particle. We also give a qualitative discussion of the general transmission line shape, and discuss quantum oscillations of the CRI propagation.

A. Dimensional Resonance

1. *Dependence on Carrier Concentration*

Variation of the dimensional resonance with car-

rier concentration was studied in a powder of relatively pure InSb having grain diameters $88 < d < 105$ μm. By varying the temperature of the powder *in situ*, it was possible to vary the carrier concentration in known fashion in the range $n > 10^{16}$ cm^{-3}, where dimensional resonance is expected at moderate field values. Figure 6 shows experimental transmission data through the undiluted powder for three temperatures above room temperature (solid curves). The dashed lines show the same data taken at higher gain settings so that the positions of resonance are more accurately defined. The circles represent theoretical computer calculations, to be discussed later. As the temperature increases, from lower to upper curves, the resonance shifts to higher CRA magnetic fields, as is predicted by
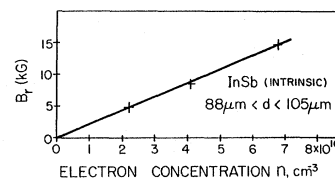

FIG. 7. Position of the size-dependent resonances in Fig. 6 vs electron concentration. Note the linear dependence, expected for dimensional resonance.
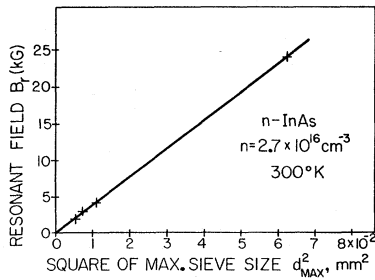
FIG. 8. Relation of the experimental position of size-dependent resonance to the square of maximum nominal particle diameter. This is the behavior expected for dimensional resonance.

Eq. (29), since increasing temperature is accompanied by increasing carrier concentration. We recall that, although the material is intrinsic, κ' is primarily determined by the electron plasma under condition $\mu_p B < 1$, as has been demonstrated in helicon experiments on corresponding bulk samples.[24]

Using the known variation of carrier concentration with temperature for intrinsic InSb,[25] we obtain Fig. 7, which shows that the resonance fields in Fig. 6 increase accurately as the first power of electron concentration, as predicted by Eq. (29). Quantitatively, the single-sphere prediction has a slope 38% less than the line drawn through the data, largely due to the neglect of pulling effects, noted in Sec. IV A 3.

2. Dependence on Particle Size

The size dependence of dimensional resonance in granular media was investigated in InSb and InAs by crushing previously characterized single-crystal specimens and size fractioning, as described in Sec. II. Figure 8 shows that the resonance fields observed in powder transmission increase precisely as the square of powder particle size, in accordance with Eq. (29). In this case, we have plotted the resonance field against the nominal maximum particle size because, according to Eq. (30), the strength of resonance absorption increases rapidly with particle diameter. In this case, the single-sphere prediction has a slope 24% less than the line shown through the data (see Sec. IV A 3).

At this point, we return to Fig. 1(b), which shows the behavior of an unsifted powder, containing a large range of particle sizes. The apparent reversal of handedness (inasmuch as the powder transmits the circular polarization for which the single-crystal slab is opaque, and *vice versa*) has a simple explanation in terms of dimensional resonance and the size dependence just discussed. In the CRA configuration, the large range of particle sizes in an unsieved powder provides resonant absorptions at all CRA field values and renders the

sample opaque at those fields. At each field value the powder behaves like a collection of strongly absorbing *magnetic* dipoles (see Fig. 5) circularly rotating about the applied field in the CRA direction.[26] In this sense the powder, formed from nonmagnetic material, can be viewed as a continuous medium whose electrodynamic response is determined by a macroscopic magnetic *permeability*.

In the CRI configuration, the wavelength inside the particles is large and the decay length small, so that the waves are largely rejected by the particles, as discussed in Sec. III A 4. The first layer of particles is excited by the incident circularly polarized wave, which induces currents around the surfaces of the particles. These currents absorb some energy in accordance with Eq. (16) but (being good reflectors when $\kappa' < 0$) reradiate a great deal and thus excite the next layer of particles, and so on. In this fashion appreciable CRI energy passes through the powder relative to the CRA case.

Figure 9 illustrates that the "reversed handedness" occurs in many materials, here n-type InAs, InSb, and HgTe. The basic requirement is that the electron concentration be high enough to give dimensional resonances for waves of the CRA configuration. The structure, particularly conspicuous
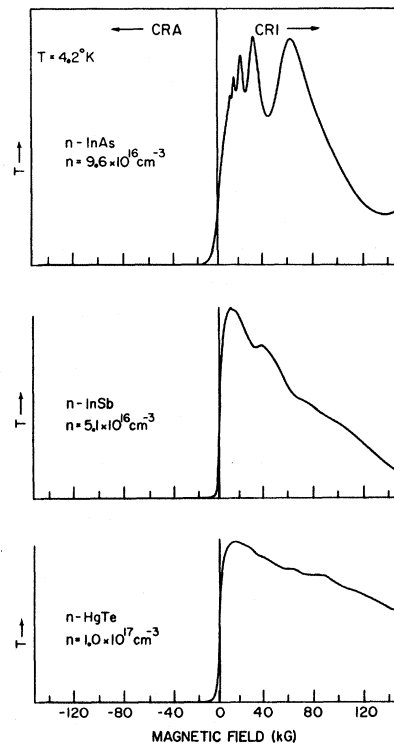

FIG. 9. Transmitted power T through unsieved powders of three different n-type semiconductors, all showing similar behavior, especially the "reversal of handedness." The scale of T is arbitrary, with peak transmissivity of 0.1 to 1.0% for samples 8 mm thick.
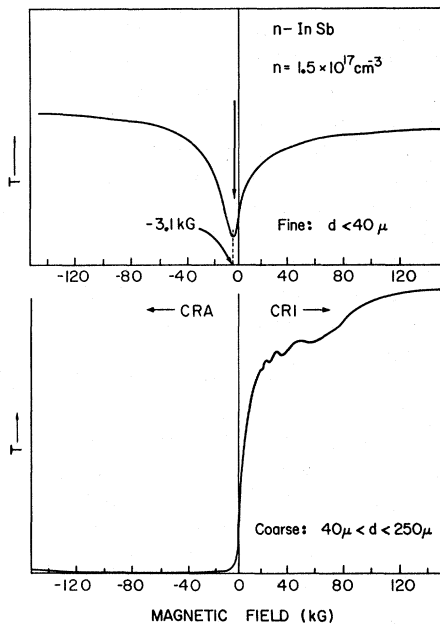
FIG. 10. Transmission through fine and coarse fractions of a highly doped *n*-type InSb powder. The well-defined dimensional resonance in the upper curve is associated with the largest particles in the fine powder. Gain for the lower curve is 10 times that for the upper curve, using samples of the same thickness (8 mm).

in the CRI transmission of the *n*-type InAs powder, is due to the Shubnikov–de Haas effect in this material, to be discussed in Sec. IV B 3.

It is also of some interest to note that sharp dimensional resonance can be seen in a powder of broad particle distribution, as long as the maximum particle size is not too large. This is exemplified in Fig. 10, showing the transmission of an *n*-type InSb powder which has been divided into two fractions: particles with diameter less than 40 μ (the upper curve); and particles greater than 40 μ, up to 250 μ (the lower curve). The coarse powder in the lower curve behaves in the usual fashion of an "unsieved" powder, already discussed. The *fine* powder in the upper curve shows a well-defined resonance because the largest of the particles are just large enough to undergo dimensional resonance while the host of smaller particles are too small to resonate.

3. *Effect of Particle Interactions*

The effects of particle interaction were investigated by diluting a powder with inert material,[27] thereby enlarging interparticle separation and diminishing interaction. As expected, transmissivity decreased rapidly with increasing powder volume fraction δ. More importantly, however, the position of dimensional resonance shifted toward *higher* CRA

magnetic fields for denser distributions, as shown in Fig. 11 for a series of 1-cm-thick InAs powder samples. Note that the rate of shift appears to decrease at large values of δ. The field value for undiluted powder is $\approx 45\%$ greater than the projected value for $\delta = 0$, corresponding to an isolated particle. Particle interaction may therefore account for the fact that Eq. (29) yields values 25–40% smaller than the experimental results shown in Figs. 7 and 8.

We have subsequently studied the δ dependence of Rayleigh *magnetoplasma* resonance, where the shift is toward *lower* CRI fields.[3] This apparent difference is resolved on the unified magnetic field scale $(-\infty < B < +\infty)$ where both kinds of resonance shift in the same direction—toward more negative field values, for increasing δ.

4. *Variation of Transmissivity with Sample Thickness*

It is of considerable interest in connection with line-shape analysis to determine the variation of transmitted power with powder slab thickness. When the slab is thick compared to the skin depth of effective waves in the powder, transmissivity will decrease exponentially with slab thickness and "spectral" structure due to Fabry-Perot resonances of the powder slab can be ruled out.

Figure 12 is constructed from curves of transmissivity versus field taken on an intrinsic InSb powder for four different slab thicknesses: 0.6, 2, 4, and 8 mm. Each solid line is a linear fit to the behavior at one magnetic field for the three greatest thicknesses; the dashed curves indicate the trend for smaller thickness. The five lines represent five distinct sensitive portions of the transmissity curve (cf. Fig. 6). For thicknesses greater
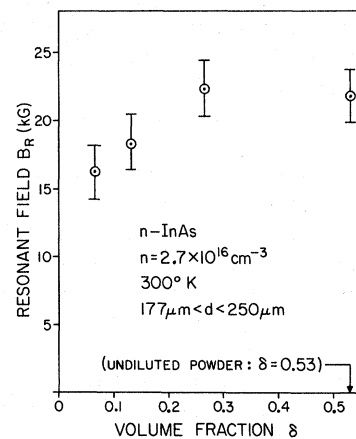

FIG. 11. Dependence of the position of dimensional resonance on the volume fraction δ of powder particles in a series of diluted samples ≈ 1 cm thick. Note that increased particle interaction associated with higher δ shifts the resonance to higher (CRA) magnetic fields.
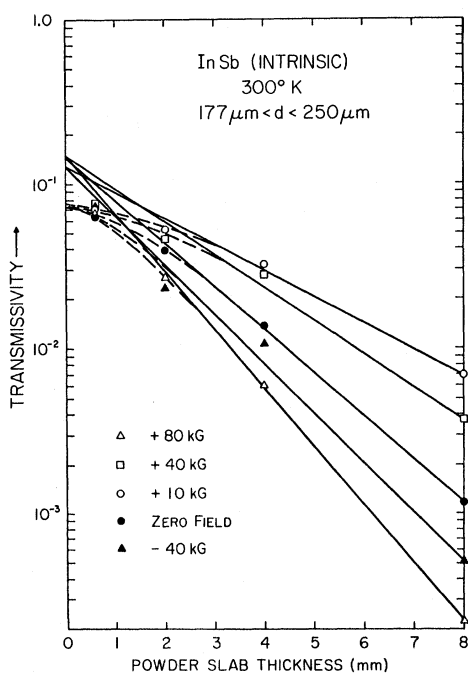
FIG. 12. Dependence of powder slab transmissivity on slab thickness at several field values. Note the approximately exponential behavior above 2-mm thickness.

than about 2 mm, the transmissivity T appears to obey the exponential relation $T = T_0 e^{-ct}$, where T_0 is independent of t and apparently only weakly dependent on B, while c is also independent of t but strongly depends on magnetic field. This conclusion supports our use of the Lambert-Beer law in the following discussion of line shapes. The reason that T_0 is less than unity is unclear; it may be associated with guided wave effects including losses and mode conversion at the rough powder interface, or other sources which we cannot identify in the present analysis.

B. General Transmission Line Shape

1. *Intrinsic Materials: Effect of Holes*

Intrinsic materials merit a more detailed discussion because they represent a special case where the entire line shape can be satisfactorily presented in terms of the Drude model, without recourse to other refinements discussed in detail in Sec. III B 2. As remarked earlier, the position of dimensional resonance in intrinsic material (where $n = p$) can be satisfactorily explained in terms of electrons only, because it is the highly mobile electronic plasma which determines κ' as long as the condition $\mu_p B < 1$ (satisfied throughout our experimental range) holds. However, as has been shown in helicon experiments on bulk intrinsic samples,[24] the presence

of holes has a drastic effect on κ'' when $\mu_p \mu_n B^2 \gtrsim 1$, a condition reached at relatively moderate fields (e.g., approximately 25 kG in intrinsic InSb at room temperature).

In powder experiments performed in the intrinsic range, discussion of the entire transmission spectrum will therefore demand consideration of the holes. Specifically, the holes are required to account for the strong absorptions observed at large CRA and CRI magnetic fields, observed in the case of intrinsic InSb, Fig. 6. Considering *electrons* only, we expect dimensional resonance at essentially the fields observed, and according to Eq. (32), we expect Rayleigh magnetoplasma resonance at fields above 800 kG in CRI configuration only. The resonance linewidth, predicted semiclassically using Eq. (31), is quite narrow, measured by $\Delta B \approx 2/\mu_n \approx 1$ kG. Furthermore, the Drude model does not predict the strong absorption at large CRA fields (beyond dimensional resonance) when electrons only are considered.

Including the holes in a semiclassical manner, we find three effects in addition to those ascribed to the presence of electrons only.[2,3] First, a second absorption maximum is predicted at large magnetic fields. This may be regarded as the residue of the magnetoplasma resonance due to holes only (which would in the absence of electrons appear at -800 kG). At the same time, the two magnetoplasma resonances are drawn together, toward field values *lower* than 800 kG by a factor of 2 or 3, because of interaction of the electron and hole plasmas in each individual grain. Finally, both absorption peaks are enormously broadened because they occur at sufficiently high fields that the hole terms dominate the imaginary part of the bulk dielectric constant κ''. The holes are about 80 times less mobile than the electrons, so the fundamental linewidths $\Delta B \approx 2/\mu_p$ are then expanded to the order of 100 kG. Thus, qualitatively, the holes appear sufficient to account for the observation of strong absorption at large CRA and CRI magnetic fields.

The effect of the electron-hole system on the high-field absorption is *quantitatively* illustrated in Fig. 6 by the circles, which represent calculated transmission, computed from the Lambert-Beer law of absorption[28]

$$T = T_0 e^{-N\Sigma t} \tag{33}$$

TABLE I. Concentrations and cgs mobilities of InSb used in Fig. 6 (Ref. 25).

T (°K)	$n = p$ (cm^{-3})	μ_n	μ_p
310	2.4×10^{16}	5.7×10^4	7.2×10^2
341	4.3×10^{16}	4.5×10^4	5.6×10^2
376	7.4×10^{16}	3.5×10^4	4.5×10^2

assuming noninteracting primarily absorptive particles. In Eq. (33) N is the number of scatterers per unit volume, t the thickness of powder sample, and Σ the total cross section of an isolated scatterer. The total cross section is taken as the sum of electric and magnetic dipole extinction cross sections $\Sigma = {}^{e}\Sigma_1 + {}^{m}\Sigma_1$ evaluated using Eq. (6), the exact Mie coefficients for spheres [Eqs. (3) and (4)], as well as the complete Drude formula for a system of electrons and holes, Eq. (19). The results are too large by about two orders of magnitude if T_0 is taken to be unity. For this reason, the theory was normalized to the data in the lowest curve (310 °K) by comparing the experimental values of $\ln(T)$ with the theoretical values of Σ. The experimental and theoretical curves were found to coincide rather well if the theoretical cross section was multiplied at all fields by a single constant differing from the experimental value of the product Nt. This procedure is interpreted as an operational correction for the neglected effects of particle interactions. The multiplicatively corrected *theoretical* quantity was used to replace $N\Sigma t$ in Eq. (33), and then T_0 was chosen so that the computed CRA peak at -40 kG had the same height as the experimental one.

Thus, with the use of only two *field-independent* adjustable parameters we obtained the fit shown at 310 °K and, with *no change* in these adjustable parameters, the theory automatically gave the excellent fits at the two higher temperatures, where only the carrier concentration ($n = p$) and the mobilities have been changed in accordance with their known temperature variation. Table I shown the concentrations and mobilities used.[25]

The systematic excess of the normalized theoretical transmission over the experimental curve appearing in the intermediate CRI fields of Fig. 6 is understood as follows: The experiments are carried out in cylindrical waveguide in the circularly polarized TE_{11} mode, whose electric field is perfectly circularly polarized *only at the center* of the guide, and everywhere else is elliptical, containing therefore some circular polarization opposite to that at the center. Thus, some of the particles nominally excited by the CRI mode are in fact also excited by an appreciable component of the CRA polarization, which is promptly absorbed in the field range roughly corresponding in magnitude to the dimensional resonance absorption of the CRA mode. For this reason, less energy passes through the powder in this range of CRI fields than predicted by CRI plane-wave theory, which assumes pure CRI polarization at every point.

2. Line Shape in Extrinsic Range: Qualitative Remarks

Discussion of the transmission line shape, away from resonance, is in general quite difficult. We

were able to accomplish this with reasonable success for intrinsic materials. In that case, however, Eq. (19) provides an adequate model for magnetoconductivity, and the complete dipole cross sections (electric and magnetic) can be calculated exactly by computer. An analytic approach is, on the other hand, complicated by the fact that the relative importance of the electric and magnetic cross sections varies with field. Attempts to relate transmission line shape in a physically revealing manner to microscopic parameters of the medium is therefore possible only in certain limiting cases. Furthermore, for the case of extrinsic semiconductor powders at high fields, where the Drude model does not provide a satisfactory description of κ'' (see Sec. III B 2), the analysis can be carried out only in a qualitative manner.

From the presentation in Sec. III it can be readily seen that whenever dimensional resonance conditions ($\alpha a \gtrsim 1$) are satisfied in the CRA mode (e.g., the entire left-hand side of Fig. 9), the CRI excitation in the corresponding field range (e.g., the right-hand side of Fig. 9) is described by Eqs. (16) and (17). Specifically, CRI transmission is then overwhelmingly determined by the magnetic dipole cross section, Eq. (16). In the helicon approximation this "large-particle behavior" can be described
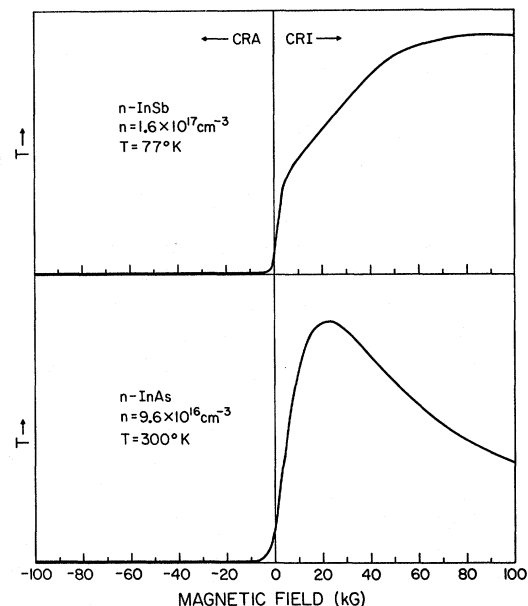

FIG. 13. Typical line shapes of transmitted power T (relative scale) for InSb and InAs well above liquid-helium temperatures. The sample parameters satisfy small skin-depth conditions of Sec. III A 4 for the CRI mode throughout the entire field range. The InAs curve does not change qualitatively as the temperature is lowered to below 77 °K. Peak T is approximately 0.1% for samples 8 mm thick in both instances.
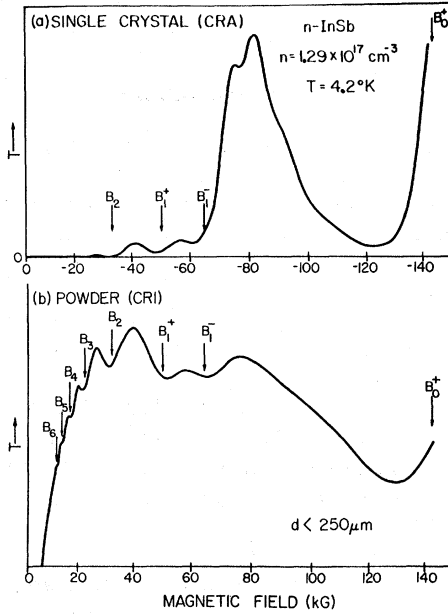
FIG. 14. Shubnikov–de Haas resonances in transmission through n-type InSb in (a) single crystal and (b) powdered form. Note the well-resolved spin splitting (B_1^+, B_1^-) in the powder data.

by

$$^m\Sigma_{\text{ext}} \approx 3\pi a^2 \frac{\kappa''}{|\kappa'|^{3/2}} \approx \frac{3\pi a^2 (\omega \epsilon_0)^{1/2}}{(ne)^{3/2}} B^{3/2} \sigma_{xx}(0, B) .$$

$$(34)$$

Before discussing the quantum oscillations in Sec. IV B 3, we consider the general trend of the nonresonant CRI transmission at high fields. We note that the transmission drops off particularly fast in the case of the InSb sample of Fig. 9, where the quantum limit is attained at about 25 kG. Beyond that point, for degenerate ionized impurity scattering,[16] σ_{xx} gradually becomes directly proportional to B, and the cross section (34) is therefore expected to increase rapidly.

In Fig. 13 we present transmission in InAs and InSb powders under similar conditions at higher temperatures. Inspection of the InAs data on the CRI side reveals that $\sigma_{xx}(0, B)$ must fall off less rapidly than $B^{-3/2}$ beyond 25 kG. Magnetic field dependence of the InSb data at 77 °K shows a more complicated behavior, suggesting a faster rate of decrease in σ_{xx}. It is to be noted that the quantum limit is not satisfied in either of the samples in Fig. 13.

3. Quantum Resonance

At low temperatures and high carrier concentrations, when degenerate statistics prevail, $\sigma_{xx}(0, B)$ displays an oscillatory character in the range ζ_F

$> \hbar \omega_c \gg k_B T$, which has been referred to as the "oscillatory region" in Sec. III B 2. In this region, σ_{xy} is still described by its asymptotic "classical" form, Eq. (27), while σ_{xx} displays sharp maxima whenever

$$\zeta_F(B) = (L + \tfrac{1}{2})\hbar \omega_c + \tfrac{1}{2} S |g| \mu_B B ,$$

$$(35)$$

according to the well-known Shubnikov–de Haas effect. Here $\zeta_F(B)$ is the magnetic-field-dependent Fermi energy, L is an integer, μ_B is the Bohr magneton, $|g|$ is the magnitude of the conduction-electron g factor, and S takes the values of $+1$ or -1 for the two spin orientations.

In the helicon approximation, where Eqs. (21) hold, it should be possible to observe clear evidence of orbital quantization in powder propagation for materials with isotropic band structure. Specifically, recalling Eqs. (16) and (23), we expect sharp oscillatory behavior in the CRI transmission under small skin-depth conditions, described in Sec. III A 4.

Figure 14 compares the oscillations seen in helicon (CRA) transmission through a single-crystal slab[29] with those seen in the CRI transmission through an unsieved coarse powder of the same material, whose particles satisfy the criteria of Sec. III A 4. The arrows mark the theoretical positions of the Shubnikov–de Haas peaks in $\sigma_{xx}(0, B)$ calculated for an InSb electron gas of the given concentration.[29, 30]
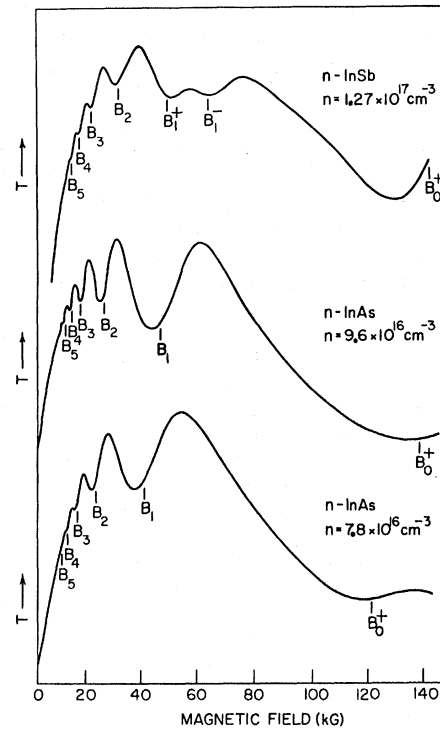

FIG. 15. Shubnikov–de Haas resonances in powdered n-type InSb and InAs of different carrier concentrations.

Note the well-resolved spin splitting (marked B_1^+ and B_1^-) of the $L = 1$ Landau level in the powder data. It is well known that Shubnikov–de Haas oscillation can be used to estimate the carrier concentration and, when spin splitting is observed, also the conduction-band g factor. The data demonstrate that such basic quantitative parameters may therefore be gotten from powder transmission experiments in suitable cases. Figure 15 shows that the effect is also seen, accurately, in n-type InAs of two different concentrations. The resolution is an indication of the high spherical symmetry of the conduction band in these materials.

It is clear from Figs. 14 and 15, which display the field values B_L corresponding to the theoretical σ_{xx} singularities[30] calculated from the known parameters for each sample, that the CRI transmission minima occur very near the maximum values of σ_{xx}, as predicted by Eq. (16). This fact is further borne out qualitatively by the spin splitting observed in the transmission minimum for $L = 1$ in the InSb data, since it is the σ_{xx} maximum which exhibits two peaks.[31] This feature is important for the following reason: At high quantum numbers one is generally concerned with the period of the oscillations rather than the absolute positions of the extrema. However, at low quantum numbers, such as in the case at hand, actual field values corresponding to the singularities of σ_{xx} are critically important in the data analysis because of the $\vec{B}$ dependence of ζ_F. A criterion for locating these field values (rather than measurement of the period of the oscillation alone) presents therefore a valuable experimental tool. For our purposes, these features also serve

to further substantiate the validity of Eq. (16) and, ultimately, of the assumptions which lead to its derivation.

V. CONCLUDING REMARKS

The approximate single-particle theory presented in this paper has proven adequate for explaining all the qualitative features of the transmissivity data observed so far. The model is such a drastic simplification of the true system that its moderate quantitative successes seem remarkable, and one is tempted to pursue the work further. Accordingly, our group is involved in efforts at several theoretical improvements, and the acquisition of new and more precise experimental data. Theoretically, we are expending further effort toward an exact solution of the single gyrotropic sphere scattering problem, as well as a multiple-scattering effective medium treatment of the particle interactions in a powder system. Experimentally, we are gathering phase and Faraday rotation data, and are attempting to relate transmissivity to reflectivity and absorptivity. In addition, we are pursuing measurements comparing the behavior in Faraday configuration with that in the ordinary and extraordinary Voigt configurations. Measurements are also planned using random aggregates of spherical grains to experimentally determine the effect of the irregular shapes found in crushed powders. It is hoped that this experimental information will enable adequate empirical extension of the single-particle and multiple-scattering theory to the very difficult region of dense distributions encountered in a real undiluted powder.

*Work supported by the Advanced Research Projects Agency. Measurements performed at the Francis Bitter National Magnet Laboratory, MIT, Cambridge, Mass. Theoretical analysis presented here constitutes part of a dissertation submitted by F. L. Galeener to Purdue University in partial fulfillment of the requirements for the Ph. D degree, June, 1970.

†Present address: Xerox Palo Alto Research Center, 3180 Porter Drive, Palo Alto, Calif. 94304.

[1]J. K. Furdyna and F. L. Galeener, in *Proceedings of the Ninth International Conference on Physics of Semiconductors, Moscow,* USSR, 1968 (Nauka, Leningrad, 1968), p. 870; F. L. Galeener and J. K. Furdyna, Appl. Phys. Letters 14, 163 (1969).

[2]For much greater detail concerning experiment and theory (except Sec. III B2) see F. L. Galeener, Ph. D. thesis (Purdue University, 1970) (unpublished), available from University Microfilms, Ann Arbor, Mich.

[3]K. K. Chen, F. L. Galeener, and J. K. Furdyna, Appl. Phys. Letters 16, 387 (1970).

[4]See, e.g., J. K. Furdyna, Appl. Opt. 6, 675 (1967), and references quoted therein.

[5]P. S. Epstein, Rev. Mod. Phys. 28, 3 (1956).

[6]H. R. Nagelberg, J. Math. Phys. 6, 44 (1965).

[7]See, e.g., Y. J. Seto and A. A. Dougal, J. Math.

Phys. 5, 1326 (1964).

[8]M. Cardona and B. Rosenblum, Phys. Rev. 129, 991 (1963).

[9]J. A. Stratton, *Electromagnetic Theory* (McGraw-Hill, New York, 1941), p. 563ff.

[10]M. Born and E. Wolf, *Principles of Optics,* 2nd ed. (Pergamon, London, 1959), p. 630ff.

[11]Perhaps the best compendium of information on small particle scattering is H. C. van de Hulst, *Light Scattering by Small Particles* (Wiley, New York, 1957); see especially Chap. 9.

[12]See, e.g., *Handbook of Mathematical Functions,* edited by M. Abramowitz and I. A. Stegun, (U. S. GPO, Washington, D. C., 1964).

[13]J. K. Furdyna and A. R. Krauss, Phys. Rev. B 2, 3183 (1970).

[14]A. C. Beer, in *Solid State Physics,* Suppl. IV, edited by F. Seitz and D. Turnbull (Academic, New York, 1963), p. 102ff.

[15]H. Weiss, in *Semiconductors and Semimetals,* Vol. 1, edited by R. K. Willardson and A. C. Beer (Academic, New York, 1966), p. 315.

[16]E. N. Adams and R. W. Keyes, in *Progress in Semiconductors,* Vol. 6, edited by A. F. Gibson (Wiley, New York, 1962), p. 85.

[17]O. Wolman and A. Ron, Phys. Rev. 148, 548 (1966).

[18]L. M. Roth and P. Argyres, in Ref. 15.

[19]The spherical Bessel functions of complex argument and low order n were calculated using a combination upward recursion and series expansion method outlined in F. L. Galeener, Ph. D. thesis (Purdue University, 1970) (unpublished).

[20]For alternative computational methods see G. W. Kattawar and G. N. Plass, Appl. Opt. 6, 1377.

[21]F. L. Galeener, Phys. Rev. Letters 22, 1292 (1969).

[22]Annotated bibliography of Rayleigh's papers on scattering has been given by V. Twersky, Appl. Opt. 3, 1150 (1964).

[23]G. Dresselhaus, A. F. Kip, and C. Kittel, Phys. Rev. 98, 368 (1955); 100, 618 (1955).

[24]J. K. Furdyna, Phys. Rev. Letters 14, 635 (1965).

[25]C. Hilsum and A. C. Rose-Innes, *Semiconducting III-V Compounds* (Pergamon, New York, 1961), curves

1 and 4 of Fig. 6.6, as well as Fig. 6.5 with theoretical extension to lower temperatures.

[26]F. L. Galeener, A. A. Saralkar, and J. K. Furdyna, Appl. Phys. Letters 17, 486 (1970).

[27]Hollow glass spheres wetted with a Teflon base adhesive: Eccospheres S1, supplied by Emerson and Cuming, Inc., Canton, Mass. and Adhesive 80, supplied by Fluoro Plastics, Inc., G and Venango Streets, Philadelphia, Penn. 19134.

[28]See, e.g., A. C. Hardy and F. H. Perrin, *The Principles of Optics* (McGraw-Hill, New York, 1932), p. 24.

[29]J. K. Furdyna, Phys. Rev. Letters 16, 646 (1966).

[30]L. E. Gurevich and A. L. Efros, Zh. Eksperim. i Teor. Fiz. 43, 561 (1962); [Sov. Phys. JETP 16, 402 (1963)].

[31]See, e.g., Kh. I. Amirkhanov and R. I. Bashirov, Zh. Eksperim. i Teor. Fiz. Pis'ma v Redaktsiya 1, 49 (1965); [Sov. Phys. JETP Letters 1, 49 (1965)].

Bound-Phonon Quasiparticle in CdS

D. C. Reynolds, C. W. Litton, and T. C. Collins

Aerospace Research Laboratories, Wright-Patterson Air Force Base, Ohio 45433

(Received 16 April 1971)

Bound optical phonons associated with the phonon-assisted I_1 (4888 Å) transition in CdS have been observed. These states arise from the bonding of an LO phonon to a neutral acceptor, which provides an attractive interaction for the phonon. The interaction is with LO phonons of small wave vector (near $\vec{\kappa} = 0$). Both the Γ_1 and Γ_5 LO phonons, which result from a splitting due to anisotropic short-range interatomic forces, are observed in the bound states. The optical transitions described in this paper are similar to those described by Dean *et al.*, which involved optical phonons bound to neutral donors in GaP. The observed bound states were identified as $2S$, $2P$, and $3D$ states with measured binding energies of 26.4, 21.6, and 11.6 cm^{-1}, respectively.

I. INTRODUCTION

Phonon interactions with both free and bound excitons as well as other types of optical transitions in CdS have been reported by a number of investigators[1-5] over a period of more than two decades. Electron-phonon and exciton-phonon interactions are, indeed, quite strong in highly polar crystals, such as CdS, whose Fröhlich[6] polaron coupling constant is $\alpha \cong 0.7$, where

$$\alpha = \frac{e^2}{\sqrt{2}} \left(\frac{1}{\epsilon_\infty} - \frac{1}{\epsilon_0} \right) \left(\frac{m^*}{\omega_0 \hbar^3} \right)^{1/2} .$$

In CdS, as in other polar materials, phonon interactions with optical transitions are strongest of all for the LO phonons. But, among the many optical transitions observed in this material, it is the I_1 transition which shows the strongest interaction with the LO phonon. The I_1 transition in CdS has been identified as an exciton bound to a neutral acceptor site,[5] and it has been observed

to couple to both the Γ_1 and Γ_5 LO phonons.[7]

Optical transitions have been observed in a number of ionic crystals[8-10] in which the energy separating the parent transition and its LO phonon sideband is less than the LO phonon energy $\hbar \omega_0$ by approximately 10%. In absorption spectra of AgBr : I transitions associated with the bound exciton occur at energy separations approximately 30% less than $\hbar \omega_0$. Several theories[11-13] have been produced in terms of which these results can be explained, bearing mostly upon the bound-phonon quasiparticle model.

Toyozawa and Hermanson[11] have described a quasiparticle consisting of the exciton-phonon bound state. They have calculated binding energies and oscillator strengths for this new quasiparticle which can account for phonon interactions whose energies are less than that of the LO phonon, $\hbar \omega_0$. Recently Dean *et al.*[14] have observed LO phonons bound to neutral donors in both Raman-scattered and luminescence spectra of GaP crystals, which were doped with S, Te, Si, and Sn.
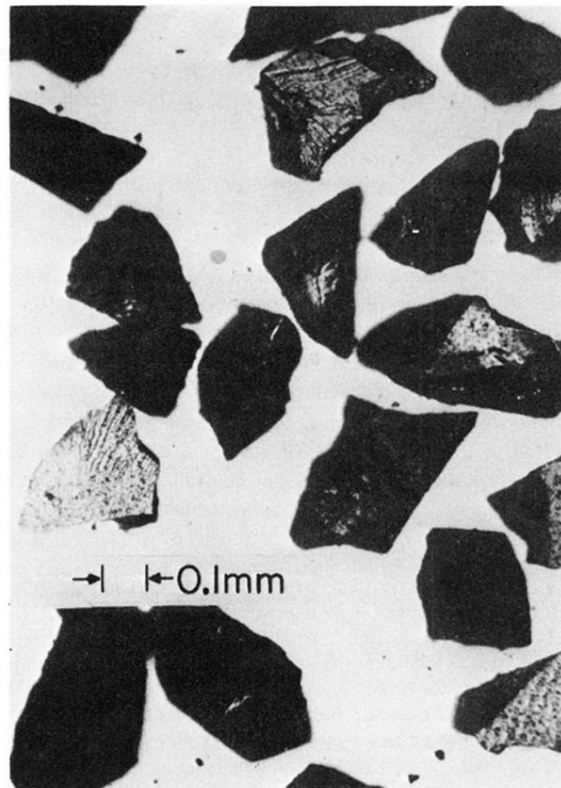
FIG. 3. Typical shape of the particles in an InAs pow-
der with nominal size range $177 < d < 250\,\mu m$. Note the
absence of noncompact shapes such as disks or needles.